



# Full-field thickness measurement of ultrathin liquid film in receding contact-induced nano-channel using surface plasmon resonance

ILTAI (ISAAC) KIM,<sup>1,\*</sup> SOKWON PAIK,<sup>1,2</sup> YANG BAE JEON,<sup>1</sup> JAE SUNG PARK,<sup>1</sup> HYUNJUNG KIM,<sup>3</sup> AND HONGCHUL KIM<sup>3</sup>

<sup>1</sup>6300 Ocean Dr. Unit 5797, Department of Engineering, College of Science and Engineering, Texas A&M University –Corpus Christi, Corpus Christi, TX 78412-5797, USA

<sup>2</sup>265 Wonhyo-ro, Unix, Yongsan-gu, Seoul 04314, South Korea

<sup>3</sup>442-13 Sandaewon-dong, CEKO, Jungwon-gu, Seongnam-shi, Gyeonggi-do 13202, South Korea

\*[ikim@tamucc.edu](mailto:ikim@tamucc.edu)

**Abstract:** This research demonstrates that a surface plasmon resonance (SPR) imaging technique can effectively measure full-field nanoscale thickness of a liquid water film filled in the receding contact-induced nano-channel. To the authors' knowledge this has not been demonstrated previously. Experimental calibration has been conducted by measuring surface plasmon resonance reflectance depending on the piezometer-controlled water nano-film thickness and comparing the experimental results with the theoretical calculations to show very good agreement. The measured full-field thickness profiles significantly visualize the three-dimensional nano-channel formation filled with liquid water film. It shows that the sensitivity and the resolution in thickness measurement are estimated as 1.21 pixel gray level/nm and 2.5 nm, respectively. The experimentally observed resolution is around 10 nm given the uncertainty in the demonstrated full-field mapping of thickness. From this research, it is demonstrated that SPR imaging successfully measures the thickness of ultrathin liquid film especially below 85 nm in full-field under normal conditions and can effectively characterize the three-dimensional nano-channel formation during the receding contact process.

© 2018 Optical Society of America under the terms of the [OSA Open Access Publishing Agreement](#)

**OCIS codes:** (240.6680) Surface plasmons; (240.0240) Optics at surfaces; (120.3940) Metrology; (240.0310) Thin films.

## References and links

1. M. Sujanani and P. C. Wayner, Jr., "Microcomputer-enhanced optical investigation of transport processes with phase-change in near-equilibrium thin liquid-films," *J. Colloid Interface Sci.* **143**(2), 472–488 (1991).
2. S. J. Gokhale, J. L. Plawsky, P. C. Wayner, Jr., and S. DasGupta, "Inferred pressure gradient and fluid flow in a condensing sessile droplet based on the measured thickness profile," *Phys. Fluids* **16**(6), 1942–1955 (2004).
3. L. Ma and J. Luo, "Thin film lubrication in the past 20 years," *Friction* **4**(4), 280–302 (2016).
4. R. P. Glovnea, A. K. Forrest, A. V. Olver, and H. A. Spikes, "Measurement of sub-nanometer lubricant films using ultra-thin film interferometry," *Tribol. Lett.* **15**(3), 217–230 (2003).
5. H. Verschuere, "Interference reflection microscopy in cell biology: Methodology and Applications," *J. Cell Sci.* **75**, 279–301 (1985).
6. D. Axelrod, "Total internal reflection fluorescence microscopy in cell biology," *Traffic* **2**(11), 764–774 (2001).
7. K. Giebel, C. Bechinger, S. Herminghaus, M. Riedel, P. Leiderer, U. Weiland, and M. Bastmeyer, "Imaging of cell/substrate contacts of living cells with surface plasmon resonance microscopy," *Biophys. J.* **76**(1), 509–516 (1999).
8. S. Granick, "Motions and relaxations of confined liquids," *Science* **253**(5026), 1374–1379 (1991).
9. S. Granick, S. C. Bae, S. Kumar, and C. Yu, "Confined liquid controversies near closure?" *Physics (College Park Md.)* **3**, 73 (2010).
10. D. F. Kienle and T. L. Kuhl, "Density and phase state of a confined nonpolar fluid," *Phys. Rev. Lett.* **117**(3), 036101 (2016).
11. C. B. Tibirićá, F. J. do Nascimento, and G. Ribatski, "Film thickness measurement techniques applied to micro-scale two-phase flow systems," *Exp. Therm. Fluid Sci.* **34**(4), 463–473 (2010).
12. B. Marchon, T. Pitchford, Y.-T. Hsia, and S. Gangopadhyay, "The head-disk interface roadmap to an areal density of 4 Tbit/in<sup>2</sup>," *Adv. Tribol.* **213**, 501086 (2013).

13. R. Advincula, E. Aust, W. Meyer, and W. Knoll, "In situ investigations of polymer self-assembly solution adsorption by surface plasmon spectroscopy," *Langmuir* **12**(15), 3536–3540 (1996).
14. L. E. Bailey, D. Kambhampati, K. K. Kanazawa, W. Knoll, and C. W. Frank, "Using surface plasmon resonance and the quartz crystal microbalance to monitor in situ the interfacial behavior of thin organic films," *Langmuir* **18**(2), 479–489 (2002).
15. J. Zhang, S. Dai, C. Ma, J. Di, and J. Zhao, "Compact surface plasmon holographic microscopy for near-field film mapping," *Opt. Lett.* **42**(17), 3462–3465 (2017).
16. T. Del Rosso, J. E. H. Sánchez, R. S. Carvalho, O. Pandoli, and M. Cremona, "Accurate and simultaneous measurement of thickness and refractive index of thermally evaporated thin organic films by surface plasmon resonance spectroscopy," *Opt. Express* **22**(16), 18914–18923 (2014).
17. S. Cheon, K. D. Kihm, J. S. Park, J. S. Lee, B. J. Lee, H. Kim, and B. H. Hong, "How to optically count graphene layers," *Opt. Lett.* **37**(18), 3765–3767 (2012).
18. H. Jussila, H. Yang, N. Granqvist, and Z. Sun, "Surface plasmon resonance for characterization of large-area atomic-layer graphene film," *Optica* **3**(2), 151–158 (2016).
19. D. Greszik, H. Yang, T. Dreier, and C. Schulz, "Measurement of water film thickness by laser-induced fluorescence and Raman imaging," *Appl. Phys. B* **102**(1), 123–132 (2011).
20. C. H. Hidrovo and D. P. Hart, "Emission reabsorption laser induced fluorescence (ERLIF) film thickness measurement," *Meas. Sci. Technol.* **12**(4), 467–477 (2001).
21. Y. Han, N. Shikazono, and N. Kasagi, "Measurement of liquid film thickness in a micro parallel channel with interferometer and laser focus displacement meter," *Int. J. Multiph. Flow* **37**(1), 36–45 (2011).
22. J. Hu, X. D. Xiao, D. F. Ogletree, and M. Salmeron, "Imaging the condensation and evaporation of molecularly thin films of water with nanometer resolution," *Science* **268**(5208), 267–269 (1995).
23. A. Verdaguer, G. M. Sacha, H. Bluhm, and M. Salmeron, "Molecular structure of water at interfaces: wetting at the nanometer scale," *Chem. Rev.* **106**(4), 1478–1510 (2006).
24. P. Cao, K. Xu, J. O. Varghese, and J. R. Heath, "The microscopic structure of adsorbed water on hydrophobic surfaces under ambient conditions," *Nano Lett.* **11**(12), 5581–5586 (2011).
25. C. Shi, X. Cui, L. Xie, Q. Liu, D. Y. C. Chan, J. N. Israelachvili, and H. Zeng, "Measuring forces and spatiotemporal evolution of thin water films between an air bubble and solid surfaces of different hydrophobicity," *ACS Nano* **9**(1), 95–104 (2015).
26. J. N. Israelachvili, "Thin film studies using multiple-beam interferometry," *J. Colloid. I. Sci.* **44**(2), 259–272 (1973).
27. X. Zhang, P. Tchoukov, R. Manica, L. Wang, Q. Liu, and Z. Xu, "Simultaneous measurement of dynamic force and spatial thin film thickness between deformable and solid surfaces by integrated thin liquid film force apparatus," *Soft Matter* **12**(44), 9105–9114 (2016).
28. J. Connor and R. G. Horn, "Measurement of aqueous film thickness between charged mercury and mica surfaces: A direct experimental probe of the Poisson-Boltzmann distribution," *Langmuir* **17**(23), 7194–7197 (2001).
29. I. Kim and K. D. Kihm, "Measuring near-field nanoparticle concentration profiles by correlating surface plasmon resonance reflectance with effective refractive index of nanofluids," *Opt. Lett.* **35**(3), 393–395 (2010).
30. I. T. Kim and K. D. Kihm, "Full-field and real-time surface plasmon resonance imaging thermometry," *Opt. Lett.* **32**(23), 3456–3458 (2007).
31. I. T. Kim and K. D. Kihm, "Label-free visualization of microfluidic mixture concentration fields using a surface plasmon resonance (spr) reflectance imaging," *Exp. Fluids* **41**(6), 905–916 (2006).
32. K. L. Johnson, *Contact Mechanics* (Cambridge University, 1985).
33. İ. Çomez, S. El-Borgi, V. Kahya, and R. Erdöl, "Receding contact problem for two-layer functionally graded media indented by a rigid punch," *Acta Mech.* **227**(9), 2493–2504 (2016).
34. I. Comez, A. Birinci, and R. Erdöl, "Double receding contact problem for a rigid stamp and two elastic layers," *European J. Mechanics A* **23**(2), 301–309 (2004).
35. H. Neff, W. Zong, A. M. N. Lima, M. Borre, and G. Holzhter, "Optical properties and instrumental performance of thin gold films near the surface plasmon resonance," *Thin Solid Films* **496**(2), 688–697 (2006).
36. K. A. Peterlinz and R. Georgiadis, "In situ kinetics of self-assembly by surface plasmon resonance spectroscopy," *Langmuir* **12**(20), 4731–4740 (1996).
37. P. Yeh, *Optical Waves in Layered Media* (John Wiley & Sons, 1998).
38. O. S. Heavens, "Measurement of the thickness of thin films by multiple-beam interferometry," *Proc. Phys. Soc. B* **64**(5), 419–425 (1951).
39. E. Hecht, *Optics*, 4th ed. (Addison and Wesley, 2002).
40. I. Kim and K. D. Kihm, "Unveiling hidden complex cavities formed during nanocrystalline self-assembly," *Langmuir* **25**(4), 1881–1884 (2009).
41. S. J. Kline and F. A. McClintock, "Describing uncertainties in single-sample experiments," *Mech. Eng.* **75**, 3–8 (1953).
42. M. Piliarik and J. Homola, "Surface plasmon resonance (SPR) sensors: approaching their limits?" *Opt. Express* **17**(19), 16505–16517 (2009).
43. Hamamatsu Data sheet of CMOS Camera, "ORCA-Flash4.0 V2", [https://www.hamamatsu.com/resources/pdf/sys/SCAS0080E\\_C11440-22CU\\_tec.pdf](https://www.hamamatsu.com/resources/pdf/sys/SCAS0080E_C11440-22CU_tec.pdf).

## 1. Introduction

Ultrathin film thickness measurement has been a substantial task in various applications such as evaporating liquid film [1, 2], thin film lubrication [3, 4], biological cell-substrates interaction [5–7] and confined liquid film [8–10]. In phase change heat transfer, the liquid film thickness is one of the critical parameters determining the heat flux coefficient, the dispersion force, and the pressure difference between liquid and vapor [1, 2]. Phase change heat transfer has become important because micro-scale heat transfer can achieve high efficiency by increasing its area-to-volume ratio in small scale and high power electronics [11]. The monitoring of thickness is one of the key parameters in thin film lubrication to understand its phenomena and predict the performance [3, 4, 12]. The quantitative measurement of the separation distance between cell and substrate is important in biology to understand cell movement and adhesion [5–7]. The measurement and control of ultrathin film thickness is crucial in confined liquid films. Such films play an important role in near-surface phenomena such as cell membranes, lubricated systems and porous materials for their non-continuum characteristics, different from the bulk liquid values, which has been an issue for decades [8–10].

Various techniques have been employed to measure thin film thickness. For solid-state samples, interference reflection microscopy (IRM) [5], fluorescence internal reflection fluorescence microscopy (TIRFM) [6] and surface plasmon resonance spectroscopy [7, 13–18] have been applied, while for the liquid-state samples, fluorescence intensity measurement [19, 20], laser focus displacement [21], atomic force microscopy (AFM) [22–25], fringe equal chromatic order (FECO) interferometry [26–28] and ultrathin film interferometry [3, 4] have been used.

IRM uses the polarized light to measure the proximity of an object to the substrate and has been used to determine the separation distance of a cell from a surface [5]. TIRFM uses the evanescent wave in total internal reflection configuration with fluorescent particles to identify the location of fluorescently labeled objects [6]. SPR spectroscopy has been effectively applied in the measurement of the nanoscale thickness of ultrathin samples in the solid state because of high sensitivity and label-free detection [7, 13–18], but not much in the liquid state and mostly pointwise. The fluorescence intensity technique was applied to measure liquid film thickness in tens micron resolution [19, 20]. The laser focus displacement method was adopted to measure liquid film thickness within the range of 2 to 140  $\mu\text{m}$ , with a resolution of 0.01  $\mu\text{m}$  [21]. AFM is known to provide high resolution for water film thickness measurement [22–25], but limited by slow speed because of the scanning method. FECO interferometry, a principle of surface force apparatus (SFA), requires elaborate image processing of fringe analysis with applications of evaporating liquid films [1, 2] and nanometer-scale thickness measurement [26–28]. Ultrathin film interferometry is applied to measure the thickness of liquid lubricants with nanometer resolution in point-wise [3, 4].

In this research, we experimentally demonstrate, for the first time to the authors' knowledge, the full-field thickness measurement of ultrathin water film filled in the receding contact-induced nano-channel in tens-nanometer resolution using a SPR imaging technique [29–31]. This technique might be applied to study evaporating thin liquid films [1, 2], nanoscale thin film lubrication [3, 4, 12], confined film characterization [8–10] and contact mechanics [32–34]. A nano-channel is formed by the receding contact process [32–34] with the four different slopes by controlling the applied forces and Fizeau interferometry technique is also employed to verify the nano-channel formation. Experimental calibration is also successfully demonstrated between the measured reflectance and the controlled thickness with uncertainty analysis, showing a very good agreement between experiment and theory. The sensitivity and resolution are estimated based on the calibration experiment. SPR imaging provides effective three-dimensional visualization of liquid-film formation in the receding contact-induced nano-channel. Furthermore, the measured contact length shows agreement with the contact mechanics theory.

### Theory for SPR liquid thin film thickness

Surface plasmon resonance imaging is highly sensitive to the dielectric constant and the effective thickness of the sample on the noble metal film in Kretschmann configuration, which is why it has been developed and applied in full-field and in situ visualization. The governing equation for SPR thin film thickness measurement is based on Fresnel reflection which is a function of the substrate (prism), the metal film (Au film), the water thin film, and the top medium. By varying the thickness of the water film with the other non-varying parameters, the reflectance,  $R$  is calculated as a function of the water film thickness. Detailed SPR theory can be found in the previous papers [17, 29–31, 35–37]. SPR imaging detects the reflected intensity at a fixed angle with the advantages of in situ and full-field detection. The reflectance,  $R$  is theoretically obtained from the four-layer system based on the transfer matrix formulation [17, 35–37];

$$R = \frac{r_1[1 + \exp(-2ik_2d_2)] + [r_1r_2 + \exp(-2ik_2d_2)]r_3 \exp(-2ik_3d_3)}{1 + r_1r_2 \exp(-2ik_2d_2) + [r_1r_2 + \exp(-2ik_2d_2)]r_3 \exp(-2ik_3d_3)}, \quad (1)$$

where  $r_i$  is the reflection coefficient between the  $i$ th and  $(i + 1)$ th layers and  $k_i$  is the wavevector in each layer. The subscript  $i = 1, 2, 3$ , and 4 refers respectively to the SF10 prism ( $n_1 = 1.732$ ), the Au thin film ( $d_2 = 47.5$  nm and  $n_2 = 0.1851 + 3.423i$ ), the water thin film ( $d_3 = t = 0 \sim 1000$  nm and  $n_3 = 1.332$ ), and the glass ( $n_4 = 1.515$ ) as in Fig. 1. The simulation was done using custom-designed Matlab code, as demonstrated in the corresponding author's previous study [29–31].

## 2. Experimental setup

The experiment was conducted under normal conditions: 21 °C and 60% relative humidity. The experimental setup consisted of surface plasmon resonance (SPR) imaging based on Kretschmann's configuration and the authors' previous study [29–31]. The SPR imaging setup (Fig. 1(a), the left) consists of the Au thin film with a thickness of 47.5 nm on an SF 10 slide glass (Phasis), a white light source (DC-950 150W quartz halogen lamp) equipped with light guide (3/8"), a 633 nm bandpass filter (FWHM 10 nm), a 16 bit (2048 × 2048 pixels) CMOS camera (Hamamatsu ORCA-Flash4.0 V2), a polarizer (Newport), a plano-convex lens for collimation (focal length of 200 mm), a SF 10 prism (Esco Optics), and a Zoom imaging lens (Edmund optics 7x precision lens) [29–31]. All parts were mounted on anti-vibration optical table (Newport SmartTable) to minimize the external vibration effect. The beams were collimated using the plano-convex lens in order to have parallel beams through the sample. The beam divergence was measured at less than 0.3 degree.

Figure 1(b) shows the experimental schematic to demonstrate how SPR can effectively measure the thickness of a liquid nano-film in full-field and nanoscale in the receding contact-induced nano-channels. Initially 50  $\mu$ l of deionized water is put on Au-coated glass slide, and a cover glass (0.17 mm thickness) is then placed on it. A spherical aluminum bead (3.175 mm in diameter) is pressed on the cover glass with different forces which are applied using the solid steel weights connected to the bead. The applied weights are weighed by putting the bead on the scale directly instead of the nano-channel. Additional water is provided through the side of the cover glass to prevent drying during measurement.

In Fig. 1(b), nano-channels are formed during the receding contact process [32–34], in which the cover glass is lifted very slightly when it is compressed by the aluminum bead and water is already filled in between the cover glass and gold film. As the bead first contacts the cover glass (1st contact), it creates stress on the cover glass. This generated stress presses the cover glass on the Au film (2<sup>nd</sup> contact) and lifts the outer edges of the cover glass [32–34]. The nano-channel thus formed shows increasing slope with increasing applied forces, as measured by SPR imaging and Fizeau interferometry. This receding contact process [32–34] offers a simple way to make nanoscale channel for the near-surface phenomena.

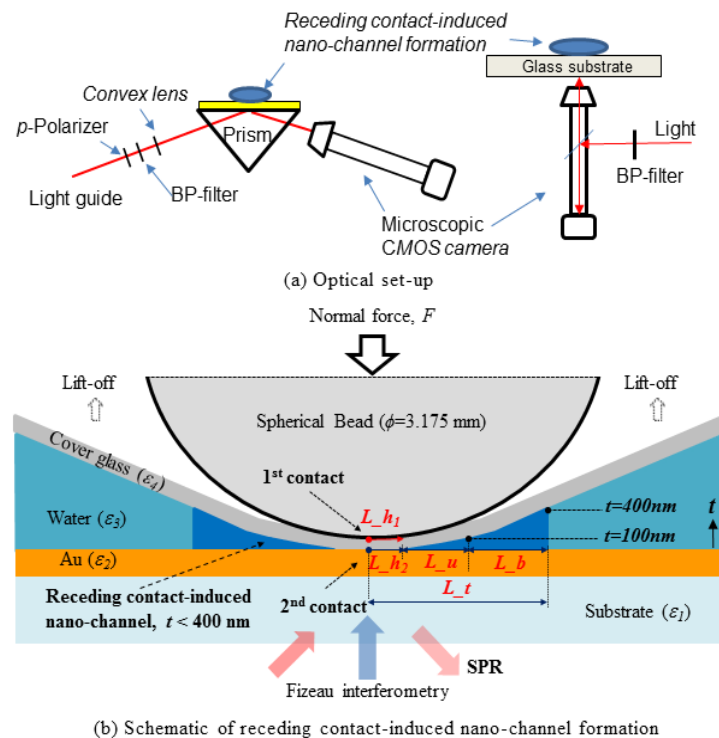


Fig. 1. Experimental set-up.

The contact stress can affect the flatness of the Au film. The extent of the Au film deformation relates to the surface condition of the deformed cover glass as well as the contact area between the Au film and the cover glass. The deformed Au film can influence the pathway of reflected light and thus the intensity in SPR imaging is distorted partially by the optical aberration.

SPR images are recorded sequentially to show the different water nano-film thickness profiles in full-field depending on the different nano-channels for different applied forces (21.6, 41.2, 60.8, and 80.4 N). In the current SPR configuration, the thickness above 400 nm is regarded as the bulk water region because the reflectance doesn't change above that thickness, as shown in the following experimental calibration experiment (Fig. 2). For background correction of raw SPR images the background image is recorded in the bulk water thickness, without any force acting on the cover glass.

Furthermore, Fizeau interferometry [38–40] is employed using a custom-designed inverted reflection microscope in order to verify the thickness of the water film in the receding contact-induced nano-channel (Fig. 1(a), the right). To achieve high resolution in thickness measurement, three different wavelengths are used sequentially with three different bandpass filters (Thorlabs; FWHM 10 nm) mounted in front of a white light: blue (450 nm), green (550 nm) and red (650 nm). 85 nm is the minimum thickness the current Fizeau interferometry configuration can measure.

### 3. Experimental calibration and analysis of uncertainty and sensitivity

#### Experimental calibration

Experimental calibration was conducted to verify the correlation between the measured SPR reflectance and the nano-film thickness through the experiment and the theory mentioned in the introduction. Figure 2 shows the experimental calibration curve between surface plasmon

reflectance and water nano-film thickness, which shows a very good agreement with the theoretical calculation. For calibration purposes, the water is on top of an Au film and a glass sphere bead (the radius is 12.6 mm) is approached from the far field to contact, where the SPR intensity no longer changes, by using a nano actuator (Newport PZA 12) with 10 nm resolution. This piezo actuator employs a non-resonant piezo micro-stepping motor. The reflectance was averaged for the center region of interest (ROI)  $50 \times 50 \mu\text{m}$  in the recorded SPR images and normalized between the maximum and minimum reflected intensities. Several representative images are shown in Fig. 2, showing good contrast depending on the thickness. Ten images are averaged for each data. The error bar is indicated for each datapoint using the standard deviations for the 10 different images, providing the consistency level out of the different measurements; it shows the acceptable consistency below the thickness of 100 nm and some large deviation above the thickness of 100 nm. The inset SPR images show SPR reflectance-thickness curve is used to determine the nanofilm thickness profile in full-field (Figs. (5) - (9).)

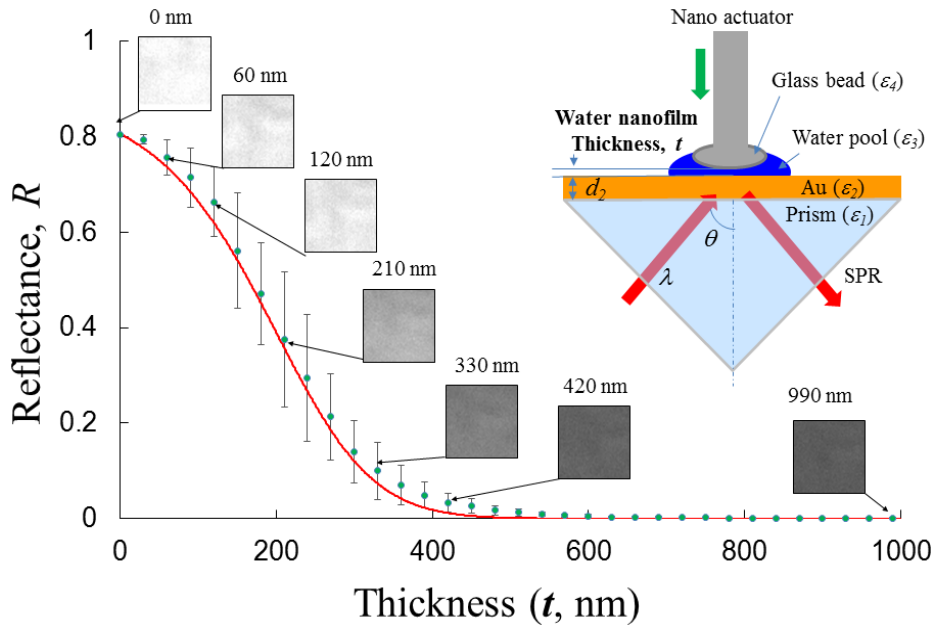


Fig. 2. Calibration curve between the reflectance and the liquid thickness. The error bar is the standard deviation for the 10 different measurements.

### Uncertainty analysis

Uncertainty analysis was conducted based on single point detection estimation [31, 41] in order to estimate the accuracy for the single measurement. The second-power equation referring to the measurement uncertainty of the reflectance  $R$  in Eq. (2) below is the function of the dielectric constants of the prism ( $\epsilon_1 = n_1^2 = 3$ ), the Au metal film ( $\epsilon_2 = -11.685 + i1.267$ ), the water film ( $\epsilon_3 = 1.774$ ), and the glass ( $\epsilon_4 = 2.295$ ), the thickness of the Au film ( $d_2 = 47.5\text{nm}$ ), the thickness of the water film ( $t = 0\sim 400\text{ nm}$ ), the wavelength of the incoming light ( $\lambda = 633\text{ nm}$ ), and the incidence angle ( $\theta = 57.2^\circ$ );

$$R = R(\epsilon_1, \epsilon_2, \epsilon_3, \epsilon_4, d_2, t, \lambda, \theta), \quad (2)$$

The overall uncertainty,  $\omega_R$  is defined as

$$\omega_R = \pm \left[ \left( \frac{\partial R}{\partial \varepsilon_1} \omega_{\varepsilon_1} \right)^2 + \left( \frac{\partial R}{\partial \varepsilon_2} \omega_{\varepsilon_2} \right)^2 + \left( \frac{\partial R}{\partial \varepsilon_3} \omega_{\varepsilon_3} \right)^2 + \left( \frac{\partial R}{\partial \varepsilon_4} \omega_{\varepsilon_4} \right)^2 + \left( \frac{\partial R}{\partial d_2} \omega_{d_2} \right)^2 + \left( \frac{\partial R}{\partial t} \omega_t \right)^2 + \left( \frac{\partial R}{\partial \lambda} \omega_\lambda \right)^2 + \left( \frac{\partial R}{\partial \theta} \omega_\theta \right)^2 \right]^{1/2}, \quad (3)$$

where the elementary uncertainties are estimated as:  $\omega_{\varepsilon_1} = 0.01\% \times \varepsilon_1$ ,  $\omega_{\varepsilon_2} = 1\% \times \varepsilon_2$ ,  $\omega_{\varepsilon_3} = 0.01\% \times \varepsilon_3$ ,  $\omega_{\varepsilon_4} = 0.01\% \times \varepsilon_4$ ,  $\omega_{d_2} = 1\% \times d_2$ ,  $\omega_\lambda = \pm 5 \text{ nm}$ ,  $\omega_\theta = \pm 0.3^\circ$ , and  $\omega_{d_3} = \pm 10 \text{ nm}$ .

The elementary uncertainties of the prism, the liquid medium, and the glass are regarded as negligible as their variations are very small [31]. The normalized uncertainty divided by the reflectance,  $R$  is calculated as Fig. 3. The overall uncertainty in Eq. (3) is close to 30% at the water thickness of 330 nm, however less than 1% and 9% below 90 nm and 210 nm, respectively. Table 1 shows that the incidence angle is the most dominant factor (< 26%), the thickness of the Au film < 14%, the wavelength < 6%, the dielectric constant of the Au film < 5% and the thickness of the water film < 2%. The uncertainty analysis shows that the divergence of the parallel beams is the most critical factor in the thickness measurement in the current configuration, but much less than 1% below the ultrathin film region ( $t < 85 \text{ nm}$ ), meaning the measured thickness is very reliable in the ultrathin film region.

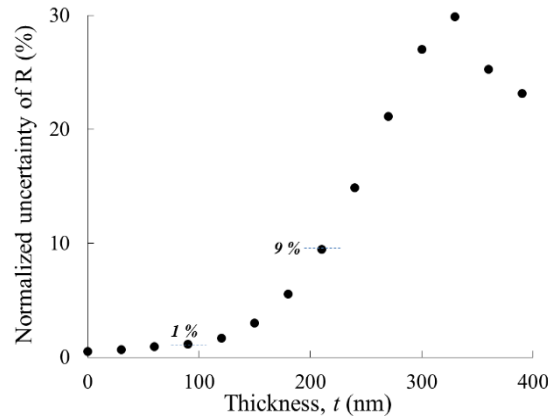


Fig. 3. Normalized uncertainty of  $R$ .

Table 1. Calculated normalized uncertainty of  $R$ .

Thickness $t$ (nm)	R	Normalized Individual Uncertainty					Normalized Overall Uncertainty
		$\varepsilon_2$	$d_2$	$t$	$\lambda$	$\theta$	
0	0.806	0.25	0.33	0.11	0.26	0.06	0.5
30	0.776	0.32	0.46	0.15	0.34	0.21	0.7
60	0.736	0.39	0.65	0.21	0.42	0.36	0.9
90	0.684	0.44	0.91	0.28	0.53	0.01	1.1
120	0.619	0.43	1.27	0.39	0.65	0.79	1.7
180	0.452	0.02	2.41	0.68	0.94	4.87	5.5
240	0.266	1.66	4.43	1.10	1.41	14.01	14.9
300	0.120	4.69	7.81	1.54	2.55	25.32	27
360	0.042	4.90	13.94	1.92	5.72	19.68	25.3

Note that the uncertainty analysis in Fig. 3 is based on single point detection with the advantage of determining which parameters are dominant in its error, while the experimental standard deviation in Fig. 2 shows the measurement consistency in multiple measurements.

### Sensitivity and resolution analysis

The sensitivity and resolution in the thickness measurement using SPR imaging were estimated using the relation suggested by Piliarik and Homola [42] with an analogue equation for the liquid film thickness. For this, one set of data is selected out of 10 measurements in the calibration experiment. Figure 4 shows the measured original intensity distribution of the single measurement and the sensitivity calculation. Each datapoint in the measured original intensity distribution shows the vertical error bar based on the calculated uncertainty in Fig. 3. The uncertainty at the thickness above 400 nm is not shown as it gets bigger with the weakening effective penetration depth of surface plasmon wave below ~400 nm [31]. The data were selected around the region with thickness < 100 nm and it shows almost linear characteristics as in the right side, which is a zoomed-in view of the left one for thickness < 100 nm. The sensitivity, based on the relation of  $S = \Delta I / \Delta t$  where  $I$  is the measured intensity in PGL and  $t$  is the thickness of the liquid film, is determined as 1.21 PGL/nm from the slope of the linear-fitting line out of the 4 datapoints (the thickness of 0, 30, 60, and 90 nm) in the right figure. The corresponding resolution ( $\sigma_t$ ) is estimated as 2.5 nm by the relation of  $\sigma_t = \sigma_o / S$  where  $\sigma_o$  is the PGL noise of the detector and  $S$  is the sensitivity.  $\sigma_o$  is 3 PGL from the manufacturer [43]. The calculated uncertainty of each data is shown to overlap a bit between some thickness ranges, for example the thickness of 30 and 60 nm, worsening the resolution to ~10 nm. It is estimated that the sensitivity and the resolution could improve by trying to reduce the uncertainty effect due to the dielectric constant of the Au film, the thickness of the Au film, the wavelength of the light, and the collimation of the light as described in the above uncertainty analysis. In addition, it is likely that the higher intensity for the zero thickness close to the saturation level (~65,000) of the detector could improve the resolution. The better thickness control (< 10 nm) could provide finer sensitivity. Furthermore, higher magnification of the objective lens is expected to provide more uniform intensity for the region of interest (ROI) of the images, decreasing the uncertainty and consequently increasing the sensitivity.

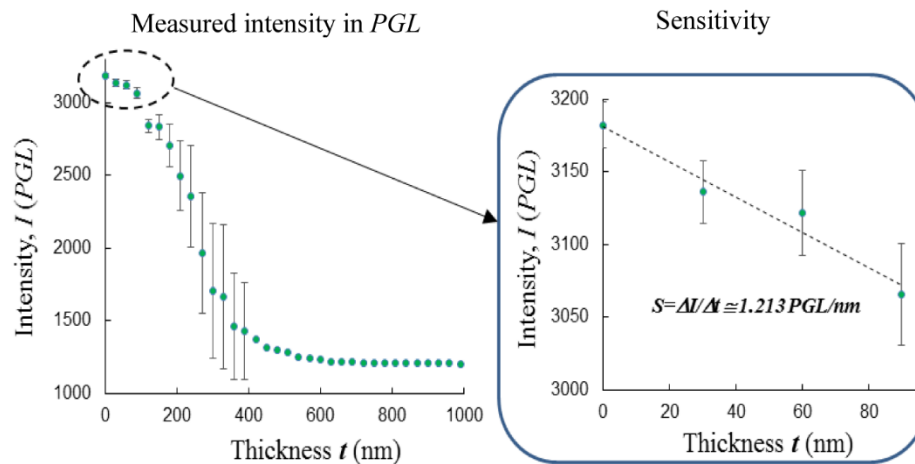


Fig. 4. Measured original intensity and its calculated sensitivity. Each data shows the vertical error bar by the calculated uncertainty (Fig. 3). The error bar for the thickness above 400 nm is not shown as the calculated uncertainty gets bigger with the weakening effective SPR penetration depth below ~400 nm [31]. Sensitivity is calculated as 1.213 PGL/nm from the slope of the linear-fitting line.

#### 4. Full-field mapping of ultra-thin liquid film thickness

Figure 5 shows raw SPR images (the top row), the centerline intensity profile (the middle row), and the thickness contour (the bottom rows) at four different slopes of nano-channels under the applied forces when a spherical aluminum bead is pressed on a cover glass under which water is already filled as in Fig. 1.

On the top row, SPR intensity proportional to reflectance increases with thinning water film thickness around the center where the cover glass is deformed by the receding contact process to form nano-scale channels. SPR images above the applied force of 41.2 N show a bright area that looks like “rabbit ear” pattern, which could be due to the deformation of the Au film. The middle row presents normalized SPR intensity profile along the centerline in SPR images denoted by a dash-dot line, which is obtained by applying background correction and 4-bit pixel binning for smoothing. 4-bit pixel binning is done by averaging the 4 neighboring pixels in the horizontal and vertical directions, respectively, to minimize the noise effect. The bottom row shows the full-field thickness contour for the bottom half of SPR images with the color range (0~400 nm), which is based on the calibration curve between the reflectance and the thickness, presented in Fig. 2 [29–31]. The region above the thickness of 400 nm is regarded as bulk water with minimum reflectance. The reflectance for the contact at zero thickness in the calibration experiment is used as the maximum. The center regions above the applied force of 41.2 N show the higher reflectance because of optical distortion and are regarded as the contact, which is why the last two images in the centerline profile are flat at the center regions. Normalization is done between the bulk water and the contact region. The thickness is determined using the experimental calibration curve. The determined thickness is then compared with the thickness from Fizeau interferogram to show a good agreement each other as in Fig. 7.

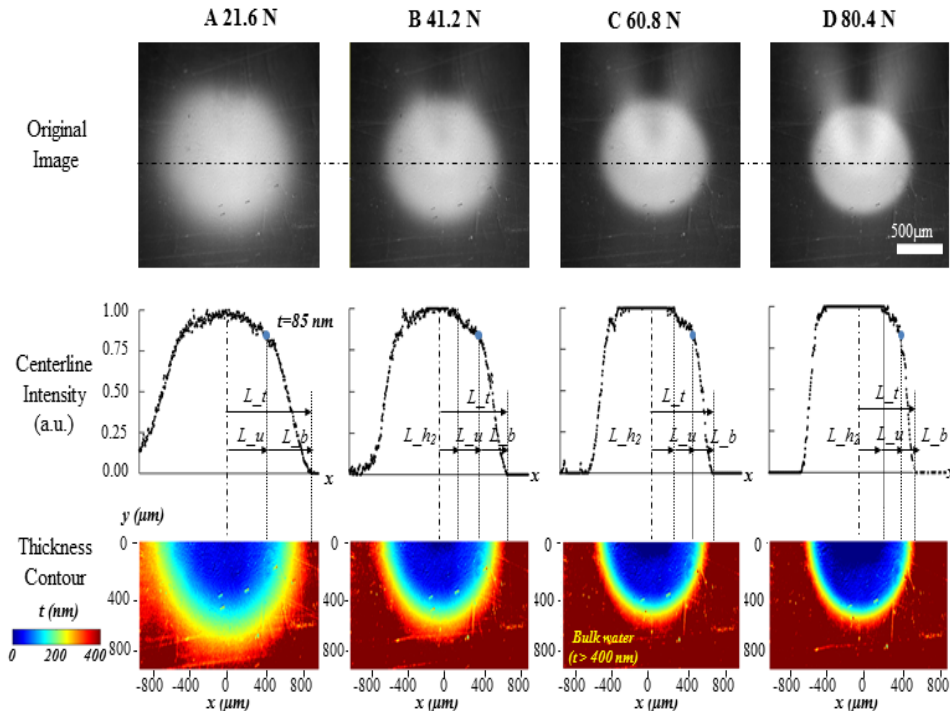


Fig. 5. SPR images and centerline intensity profiles, and liquid film thickness contours for different forces (21.6, 41.2, 60.8, and 80.4 N).  $L_{h_2}$  is the length of the 2<sup>nd</sup> hard contact region with zero thickness of water.  $L_u$  is the length of the ultrathin film region below the thickness of 85 nm.  $L_b$  is the length of buffer film region between 85 nm and 400 nm.  $L_t$  ( $= L_{h_2} + L_u + L_b$ ) is the total length from the contact center to the bulk film.

The SPR images present the broad intensity distribution in the nano-channel with the smallest slope under an applied force of 21.6 N, which is clearly shown in the thickness contour on the bottom row with the longest ultrathin film length,  $L_u$  where the thickness is below 85 nm. Fizeau interferogram in Fig. 6 also shows the same trend with the smallest number of fringes. The bulk water length between the center and the bulk water region ( $0 < t < 400$  nm),  $L_t$ , gets shorter as the applied force increases with the increasing slope of the nano-channel. The buffer film length,  $L_b$  ( $85 < t < 400$  nm) and the ultrathin film length,  $L_u$  ( $0 < t < 85$  nm) also decrease, while the contact length,  $L_{h_2}$  ( $t \approx 0$  nm) increases.

Figure 6 illustrates Fizeau interferograms with blue, green, and red bandpass filters (450, 550, and 650 nm). Three different wavelength-filters are used to increase the thickness resolution in interferometry. The interferometry measurement is done by custom-designed inverted reflection microscopy with the same magnification as in SPR imaging (Fig. 1(a), the right). The interferogram fringes show thickness profiles between the SF 10 glass substrate and the cover glass with water film in-between. The Au film is not used as the image contrast is too weak due to low transmission. The thickness is calculated as  $t_m = (m + 1/2) \lambda / 2n$  where  $t_m$  is the thickness,  $m$  is the fringe number ( $m = 0, 1, 2, \dots$ ),  $\lambda$  is the wavelength,  $n$  is the refractive index of the medium [38, 39]. For the thickness determination, the fringe pattern analysis is done for 8 directions each separated by 45 degrees around the center as the dash-lines in the 650 nm interferogram at 41.2 N. The average calculated value is shown in the centerline thickness profile of Fig. 7. The number of fringes increases with the applied forces, resulting in the thicker thickness with the increasing slope of the nano-channel, also clearly shown in Fig. 7 above the radial distance of 540  $\mu\text{m}$ . The contact length is approximated between the center point and the first fringe position, which will be discussed in more detail later in this paper.

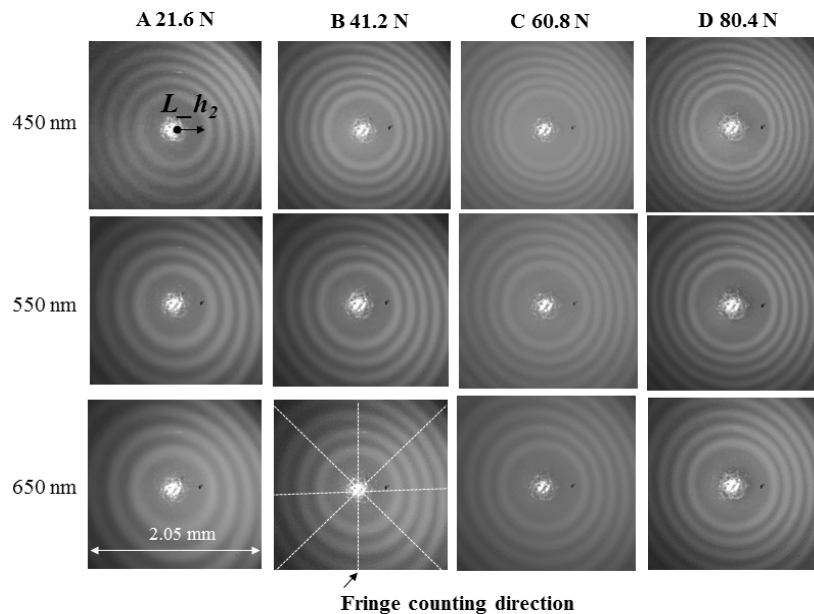


Fig. 6. Fizeau interferograms in blue (450 nm FWHM), green (550 nm), and red (650 nm) filters.  $L_{h_2}$  is the 2<sup>nd</sup> hard contact length measured between the contact center and the 1<sup>st</sup> fringe. Fringe counting direction is shown as dashed lines in 650 nm filter at the applied force of 41.2N.

Figure 7 shows the centerline thickness profile obtained from the thickness contour plot in the bottom row in Fig. 5, which is analogous to the centerline intensity profile in the middle row in Fig. 5. The measured thickness profiles from SPR are marked by red square, green

diamond, black circle, and blue triangle filled symbols for 21.6, 41.2, 60.8, and 80.4 N, respectively, while the measured Fizeau interferometry are marked by non-filled symbols. It shows good agreement between SPR and Fizeau over most thickness range. It is also shown that the thinnest thickness which Fizeau interferometry can measure at the current configuration is 85 nm due to the limitation of the applied wavelength, 450 nm.

The inset figure shows SPR measures effectively the water liquid film thickness in tens nanometer resolution in ultrathin film region less than 85 nm, which is not possible with Fizeau interferometry. The resolution of the tens nanometer is estimated due to the uncertainty effects as stated above and could be improved by reducing the uncertainty factors. Higher intensity illumination, higher magnification, and more gradual nano-channel slope are also estimated to prove the better sensitivity and resolution.

The slope lines are displayed in red, green, black and blue, showing how the nano-channel slopes increase with the applied force. The SPR thickness data within the radial distance of 100  $\mu\text{m}$  from the center at the applied force of 21.6 N, shown in red square markers in the inset figure, has a thickness distribution from 0 to 40 nm, showing the possibility of a confined water film that can support the applied force of 21.6 N [14, 15] between the cover glass and the gold surface. The receding contact mechanism enables the approach of the cover glass toward the gold film. The water between the cover glass and the gold film is squeezed out, but the water thin film could be confined between the cover glass and the gold film to be detected in SPR imaging at a thickness of a few nanometers. The applied 21.6 N is equivalent to the normal stress of 3.2 MPa on the first contact area in Fig. 1 (93  $\mu\text{m}$  of contact length calculated from the classical Hertz theory, which is explained later in this paper) between the aluminum bead ( $\phi = 3.175 \text{ mm}$ ) and the cover glass.

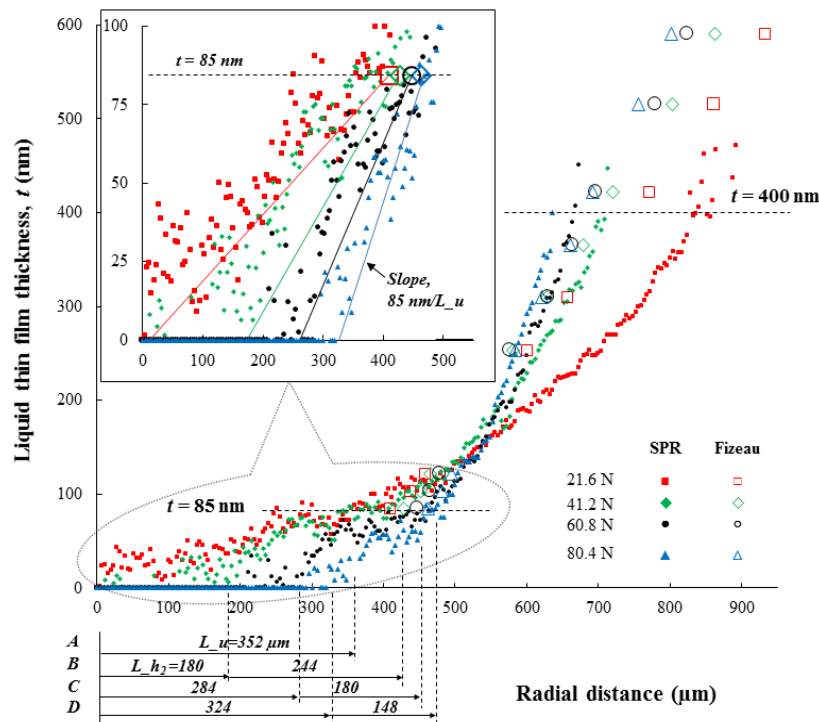


Fig. 7. Centerline thickness profile of water thin film by SPR and Fizeau interferometry depending on different applied forces; 21.6, 41.2, 60.8 and 80.4 N. The profiles by SPR are denoted by the filled symbols in square, diamond, circle, and triangle for each force, while the results by Fizeau are non-filled symbols. Online version shows colored markers in red, green, black, and blue colors. The inset figure shows the zoomed-in thickness profiles below 85 nm region. Slope lines clearly show the increasing trend with the applied forces.

The thickness profiles distinctly present the length of the ultrathin film region  $L_u$ , the slope of the nano-channel ( $85 \text{ nm}/L_u$ ), and the contact length  $L_h$ ; the decreasing ultrathin film region and the increasing slope and contact length with the applied forces. The figure also shows that the slope of the liquid film thickness gets steeper with the increasing distance from the center in each nano-channel condition, corresponding with the geometry characteristic of the spherical bead. Assuming that the sphere is in contact with a horizontal flat surface, the slope of the tangential line will increase with distance from the center.

Figure 8 effectively visualizes the three-dimensional variation of liquid film formation in the receding contact-induced nano-channel with the applied forces. The coordinates in the  $x$  and  $y$  directions are in microns and the coordinate in the  $t$  direction is in nanometers. Thus  $t$  is magnified 1000 times relative to the  $x$  and  $y$  directions. The bulk water length ( $0 < t < 400 \text{ nm}$ ),  $L_t$ , gets shorter with the increasing slope of the nano-channel due to greater lifting forces on the cover glass as in Figs. 5 and 7.

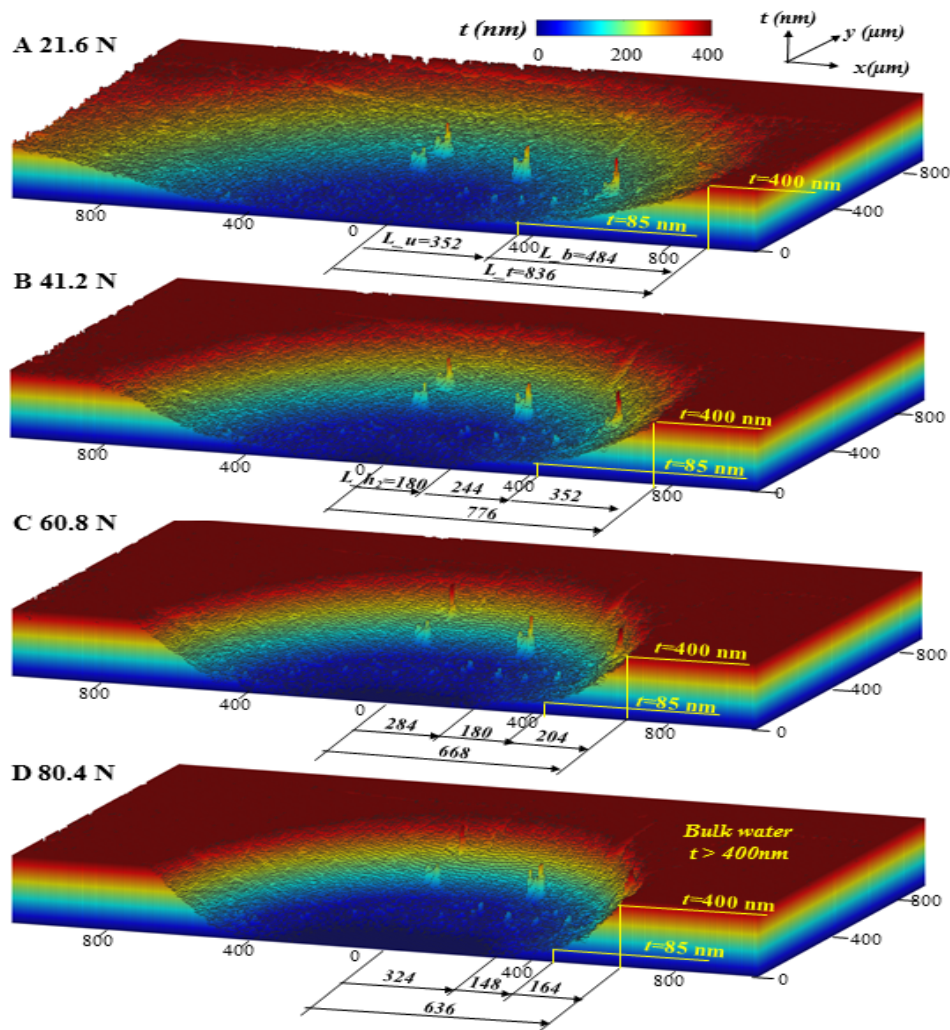


Fig. 8. Three-dimensional and full-field visualization of liquid thin film formation in the receding contact-induced nano-channel with the varying applied forces: 21.6, 41.2, 60.8, and 80.4 N. Note that the thickness,  $t$  is in nanometer and the  $x$  and  $y$  coordinates are in micron. Zero thickness is colored deep blue and the thickness above 400 nm is colored dark red.

More importantly, Fig. 8 is the full-field thickness mapping and presents the in situ imaging capability. For the nano-channel with the more gradual slope, the estimated depth resolution of 2.5 nm from the calibration experiment could be experimentally observed by reducing the uncertainties. Thus, future research could be conducted for the quantitative thickness measurement in the range below 100 nm for the study of confined liquid film existence and ultrathin evaporating film dynamics.

The SPR results show the ultrathin ( $0 < t < 85$  nm) and the contact region ( $t = 0$  nm) around the center as in Fig. 5, 7, 8, but its formation is not distinct because of the color range. Figure 9 illustrates better contrast with the narrower color range of 0~85 nm for the thickness contour on the bottom row in Fig. 5. The ultrathin film region,  $L_u$ , gets smaller: 352, 244, 180, and 148  $\mu\text{m}$  with the applied forces of 21.6, 41.2, 60.8, and 80.4 N, respectively.

The contact length,  $L_{h_2}$  regions are colored in deep blue around the center, showing the complete or hard contact of the cover glass on the Au-film as in the flat centerline thickness profile in Fig. 7. The contact length increases: 0, 180, 284, and 324  $\mu\text{m}$ . Fizeau interferogram in Fig. 6 also shows the contact region, but doesn't provide much information about the ultrathin film region.

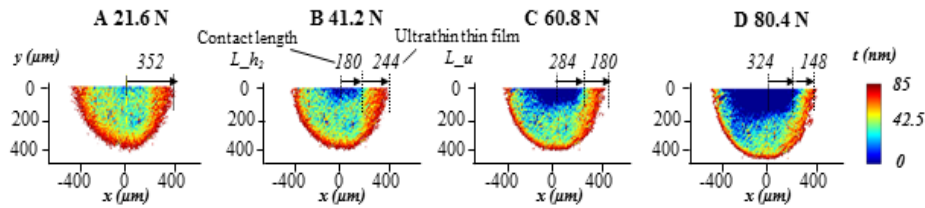


Fig. 9. Liquid film thickness contour showing ultrathin film region and contact length with the color range of 0~85 nm.

The increasing contact length with the applied force can be estimated from the contact mechanics [32–34]. The experimentally measured 2<sup>nd</sup> contact length,  $L_{h_2}$  between the cover glass and the Au film is directly affected by the 1<sup>st</sup> contact length  $L_{h_1}$ , between the aluminum sphere bead and the cover glass. The 1<sup>st</sup> contact length,  $L_{h_1}$  can be obtained with the analytical form from classical Hertz theory [32] for non-adhesive elastic contact condition as follows;

$$L_{h_1} = (3FR/4E^*)^{1/3}, \quad (4)$$

$$E^* = ((1 - \nu_{\text{glass}}^2)/E_{\text{glass}} + (1 - \nu_{\text{aluminum}}^2)/E_{\text{aluminum}})^{-1}, \quad (5)$$

where  $F$  is the applied loading,  $R$  is the radius of the spherical bead (3.175 mm),  $E^*$  is the effective elastic modulus,  $\nu_{\text{glass}}$  and  $\nu_{\text{aluminum}}$  are Poisson's ratios of glass (0.24) and aluminum (0.35), and  $E_{\text{glass}}$  and  $E_{\text{aluminum}}$  are the elastic modulus of the glass (50 GPa) and the aluminum bead (69 GPa). The calculated  $L_{h_1}$  is shown in Table 2.

The 2<sup>nd</sup> contact length,  $L_{h_2}$ , is also measured from Fizeau interferogram (450 nm) between the contact center and the position of the first fringe, which shows a longer length than SPR measurement except for the applied force of 21.6 N. The deviation between Fizeau and SPR is due to the fact that Fizeau cannot measure thickness below 85 nm.

It is known from the contact mechanics [32–34] that the current nano-channel is made by using the lift-off effect of the non-bonded cover glass on the solid substrate when the cover glass is compressed by a rigid spherical bead and the 2<sup>nd</sup> hard contact is longer than the 1<sup>st</sup> contact length. The  $L_{h_2}$  can be calculated numerically from the singular equations [33, 34] and can be graphically approximated as above 210  $\mu\text{m}$  with longer length for larger applied force. Experiment shows that the measured  $L_{h_2}$  is longer than the calculated  $L_{h_1}$  by

55~123% by SPR (except the case of 21.6 N) and ~3 times by Fizeau interferometry, respectively, which agrees fairly well with the theory. The existence of a confined liquid film might explain the deviation between SPR and the contact mechanics theory.

Table 2 shows the hard contact length comparison between the experiment and calculation, and the measured lengths for each nano-channel such as the ultrathin film, the buffer film, the bulk water, and the slope of the nano-channel.

Figure 10 shows the trend of the measured lengths of the nano-channel and the hard contact (2nd); the decreasing trend of the ultrathin film  $L_u$ , the buffer film  $L_b$ , and the bulk water  $L_t (= L_{h_2} + L_u + L_b)$ , and the increasing trend of the contact length  $L_{h_2}$ .

**Table 2. Comparison of the hard contact length and the measured lengths of nano-channels.**

			Applied force, $F$ (N)/ Normal stress (GPa)			
			21.6 / 3.2	41.2 / 3.9	60.8 / 4.4	80.4 / 4.9
Hard contact, ( $\mu\text{m}$ ) $t = 0 \text{ nm}$	Theory	1 <sup>st</sup> contact, $L_{h_1}$	93	116	132	145
		2 <sup>nd</sup> contact, $L_{h_2}$	~210 (slightly increases with increasing $L_{h_1}$ )			
	Experiment (2 <sup>nd</sup> contact, $L_{h_2}$ )	SPR	~0	180	284	324
		Fizeau	~292	~351	~368	~386
Ultrathin film, $L_u$ ( $\mu\text{m}$ ), $t < 85 \text{ nm}$		SPR	352	244	180	148
Slope ( $\times 10^{-3}$ ) in ultrathin film, $t (= 85 \text{ nm})/L_u$			0.24	0.35	0.47	0.57
Buffer film, $L_b$ ( $\mu\text{m}$ ) $85 < t < 400 \text{ nm}$		SPR	484	352	204	164
		Fizeau	~361	~292	~249	~228
Bulk water, $L_t = L_{h_2} + L_u + L_b$ $0 < t < 400 \text{ nm}$		SPR	836	776	668	636
		Fizeau	~770	~720	~696	~691

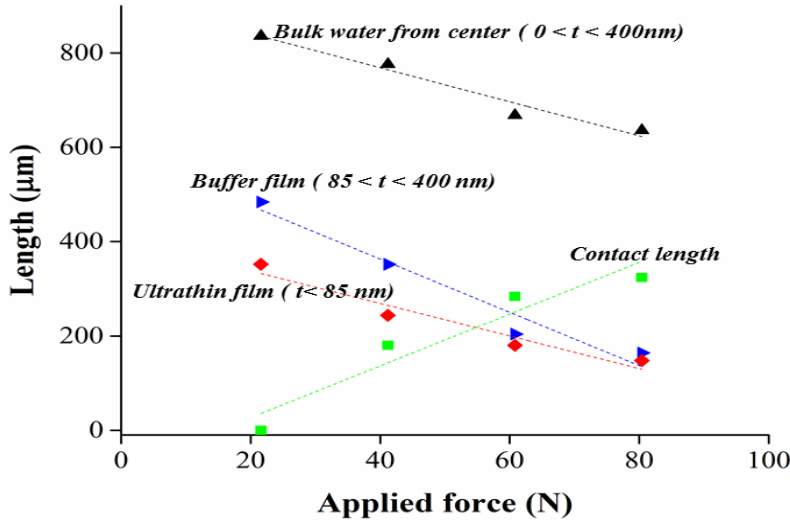


Fig. 10. Experimentally (SPR) determined lengths of the ultrathin film ( $t < 85 \text{ nm}$ ), the buffer film ( $85 < t < 400 \text{ nm}$ ), the bulk water ( $0 < t < 400 \text{ nm}$ ), the nano-channel slope ( $85 \text{ nm}/L_u$ ), and the contact length,  $L_{h_2}$ . Linearly-fitted lines are denoted for each data set.

#### 4. Summary

In this work, we successfully demonstrated that surface plasmon resonance (SPR) imaging can successfully measure ultrathin liquid film thickness with resolution of tens nanometer and full-field. Experimental calibration was conducted using a nano actuator by measuring reflectance depending on the varying thickness, to show a very good agreement between theory and experiments. The sensitivity and the resolution are estimated as 1.21 PGL/nm and

2.5 nm, respectively, from the calibration experiment. The measurement was applied to four different nano-channels formed using the receding contact process by varying the applied forces. The results show that SPR effectively visualized the liquid nano-films in the nano-channel in full-field and three-dimensions; the decreasing lengths of the ultrathin film ( $t < 85$  nm) and bulk water ( $0 < t < 400$  nm) with increasing contact length and slope of the nano-channel. The measured contact length agrees well with the contact mechanics theory that the contact length increases with the applied forces. Uncertainty analysis shows the measured thickness with less than 1% of normalized uncertainty in the ultrathin film region with the thickness below 85 nm and 30% uncertainty in the bulk water region ( $t \sim 400$  nm). The demonstrated full-field mapping of thickness shows  $\sim 10$  nm resolution due to the uncertainty. It is estimated that the resolution could experimentally reach its estimated resolution of 2.5 nanometer by reducing the uncertainty effects due to the dielectric constant of the Au film, the thickness of the Au film, the wavelength of the incoming light, and the collimation of the light. In addition, higher intensity illumination, higher magnification, more gradual slope of the nano-channel and better thickness control might improve the sensitivity and resolution. SPR imaging technique could be very effectively applied to in situ and full-field measurement of thickness variations such as confined liquid film, evaporating film dynamics, thin film lubrication, and contact mechanics phenomena.

### Funding

CEKO, Co., LTD (07032015).

### Acknowledgements

This study is also supported by Texas Comprehensive Research Fund grant from the Texas A&M University-Corpus Christi Division of Research, Commercialization.